Journal of Crystal Growth 690 (2026) 128658

Contents lists available at ScienceDirect

Journal of Crystal Growth

journal homepage: www.elsevier.com/locate/jcrysgro

Self-assembled GaAs nanostructures on 4H-SiC(0001) with ultra-thin oxide layer

Artur Tuktamyshev [a,*], Michele Gherardi [b], Luca Anzi [b], Sonia Freddi [c], Matteo Canciani [a], Stefano Vichi [a], Sergio Bietti [a], Alexey Fedorov [c], Monica Bollani [c], Roman Sordan [b], Stefano Sanguinetti [a]

[a] L-NESS and Materials Science Department, University of Milano Bicocca, Via R. Cozzi 55, Milano, 20125, Italy
[b] L-NESS and Physics Department, Politecnico di Milano, Polo di Como, Via F. Anzani 42, Como, 22100, Italy
[c] L-NESS and Institute of Photonics and of Nanotechnologies - National Researcher Council, Piazza Leonardo Da Vinci 32, Milano, 20133, Italy

ARTICLE INFO

Communicated by M. Hilse

Keywords:
Molecular beam epitaxy
Droplet epitaxy
GaAs nanostructures
SiC
Mie-resonators

ABSTRACT

We investigated a molecular beam epitaxy growth of GaAs nanocrystals on 4H-SiC(0001) substrates covered by ultra-thin oxide layer. Two growth approaches were explored: direct heteroepitaxy and droplet epitaxy. Under the standard GaAs homoepitaxy conditions, direct heteroepitaxy on SiC resulted in low-density, poorly oriented GaAs nanocrystals, likely due to limited interaction between the GaAs and the underlying crystalline SiC surface. In contrast, droplet epitaxy enabled better control over the nanocrystal density and their vertical alignment. By optimizing the arsenization conditions and the oxide layer thickness, self-catalyzed GaAs nanocrystals oriented along the [111] direction were achieved. Their lateral size is about 100 nm and the height of 150–200 nm, depending on the initial Ga droplet size and crystallization parameters (temperature and As flux). These results highlight the potential of droplet epitaxy for the integration of vertically aligned III–V nanocrystals on SiC substrates, paving the way for future nanoscale photonic applications.

1. Introduction

Modern nanophotonics offers the opportunity to enhance light–matter interaction and control the emission directivity at the nanoscale by manipulating the optically-induced Mie resonances in dielectric nanostructures with a high refractive index [1–3]. One of the applications of Mie resonators is the enhancement of exciton emission of monolayer transition metal dichalcogenides coupled with dielectric nano-antennas (DNAs) [4,5].

Dielectric resonators composed of high-refractive-index materials can be effectively integrated onto substrates with comparatively lower refractive indices, for instance, silicon dioxide (SiO_2, n ≈ 1.6), silicon carbide (SiC, n ≈ 2.6), or sapphire (Al_2O_3, n ≈ 1.8). This configuration takes advantage of the strong refractive index contrast at the interface, which promotes efficient confinement of photonic modes within the resonator structure. This enhanced confinement not only minimizes optical losses but also contributes to improved overall performance and functionality of integrated photonic devices, making this approach more suitable for a wide range of integrated photonic applications [6,7].

III–V semiconductor DNAs can be fabricated in the form of nanocolumns or nanowires (NWs) [8,9], and such nanocrystals can be implemented on different platforms due to an efficient elastic relaxation at the lateral free surface [10]. One of the extensively studied is a Si(111) substrate for the integration of III–V NW-based photonic devices with silicon-based electronics [11,12] since nanocrystals preferably grow along the [1 1 1] ([0 0 0 1]) crystallographic direction for cubic (hexagonal) crystals [8,13,14].

However, silicon while providing a compatible crystallographic template, is not a suitable substrate for the realization of III–V DNAs due to its high refractive index (Si, n ≈ 3.42) which closely matches that of typical III–V semiconductors (e.g., GaAs, n ≈ 3.3). To address this, lower-index substrates such as SiC(0001) and sapphire(0001) offer more favorable optical environments together with their C_{3v} surface symmetry similar to Si(111). While, sapphire is a well-known template for an epitaxial growth of III-N semiconductors [15], SiC has a Si-phase surface, bringing the epitaxial growth on it similar to the growth on Si(111). There are only a few reports on the epitaxial growth of III–V materials on SiC substrates. Previous studies have demonstrated the formation of AlGaAs and InGaN NWs on SiC/Si(111) templates [16,17], as well as the growth of GaAs NWs on graphene/SiC hybrid substrates [18]. More recently, two-dimensional (2D) epitaxial growth of GaAs on SiC has been achieved using a thin AlAs interlayer [19].

* Corresponding author.
E-mail address: artur.tuktamyshev@unimib.it (A. Tuktamyshev).

https://doi.org/10.1016/j.jcrysgro.2026.128658
Received 20 March 2026; Received in revised form 28 April 2026; Accepted 30 April 2026
Available online 6 May 2026
0022-0248/© 2026 Elsevier B.V. All rights are reserved, including those for text and data mining, AI training, and similar technologies.

III–V nanocolumns and NWs are grown using an Au-catalyzed, catalyst-free, or self-assisted vapor–liquid–solid (VLS) approach in molecular beam epitaxy (MBE) or chemical vapor deposition chambers [12,20,21]. A common approach to achieve well-developed vertical nanocrystals and minimize parasitic (polycrystalline) growth between them is to grow on a Si wafer covered by a thin silicon oxide layer (≈ 1 nm). In self-catalyzed or catalyst-free GaAs NW growth, Ga droplets or GaAs nanocrystals nucleate at oxide pinhole sites. These nucleation centers locally etch the oxide layer, thereby exposing the underlying single-crystal silicon substrate, facilitating vertical single-crystal growth [22,23]. Therefore, growth conditions (growth temperature and V/III ratio) and the oxide layer thickness are important to realize vertical nanocrystals [22,24].

A precise density, size, and position control of III–V nanocolumns can be achieved on patterned substrates by selective-area growth [12, 25–28]. However, the top-down approach relies on expensive instrumentation and a clean-room facility, demanding significant expertise and time. Although the density of nanocrystals and their size can be varied in wide ranges using the VLS approach, it is difficult to independently control these parameters, and the self-assembled approach results in random positions of NWs and their low uniformity of sizes [23,26]. Nevertheless, the formation of self-assembled GaAs vertical NWs with controllable density and diameter on Si(111) substrate was demonstrated via a bottom-up approach [29,30]. This method integrates two sequential growth techniques: first GaAs nanocrystal seeds are self-assembled by the droplet epitaxy (DE) [31–33] and then regrown using VLS conditions to realize high aspect-ratio NWs.

In this study, we investigated the formation of GaAs vertically-aligned nanocrystals on 4H-SiC(0001) with an ultra-thin oxide layer by the direct heteroepitaxy and the DE method in a MBE chamber. The heteroepitaxy resulted in low-density, poorly oriented GaAs nanocrystals, which is in agreement with previously reported study [19]. The control of the arsenization conditions of the DE approach led to the partial formation of low-density vertically-aligned GaAs nanocrystals, the minimization of the oxide thickness by the chemical treatment resulted in their higher quantity.

2. Materials and methods

Pieces of about 1.5 × 1.5 cm were cut from 2-inch n-type 4H-SiC(0001) wafers and cleaned in acetone and isopropanol to remove traces of dicing tape. The SiC pieces were then dried under nitrogen flux and stuck to the molybdenum sample holder using melted indium. The samples were loaded in the MBE chamber equipped with a Ga effusion cell and an arsenic valved cracker cell. The temperate of the cracker zone was set to produce As_4 tetramer molecules. Ga flux rate refers to the homoepitaxy rate on GaAs(001) substrates, which is calibrated by the reflection high-energy electron diffraction (RHEED) intensity oscillation method [34,35]. Before loading the samples into the growth chamber, the sample holder was annealed at 200 °C in the intro chamber for more than 10 h to evaporate water. After loading in the growth chamber, the samples were annealed for 15 min at 630 °C – our standard procedure to remove the rest of the water, clean the surface from the contamination, and evaporate the oxide layer from GaAs substrates. In contrast to annealing of GaAs wafer, which is conducted under As overpressure, the annealing of SiC samples was performed without As, with both the As valve and the As shutter closed. Under these conditions, the SiC oxide layer is not removed, as confirmed by RHEED. Effective oxide removal from SiC typically requires high-temperature annealing (≥ 1000 °C) [36–39], which is beyond the maximum temperature achievable with our sample heater. Using infrared pyrometer, the sample temperature T_s was calibrated by the appearance of the surface reconstruction after oxide removal on the GaAs(001) substrate at ≈ 580 °C [40], monitored by the RHEED technique. Then, T_s was controlled by the thermocouple situated between the sample holder and the substrate heater.

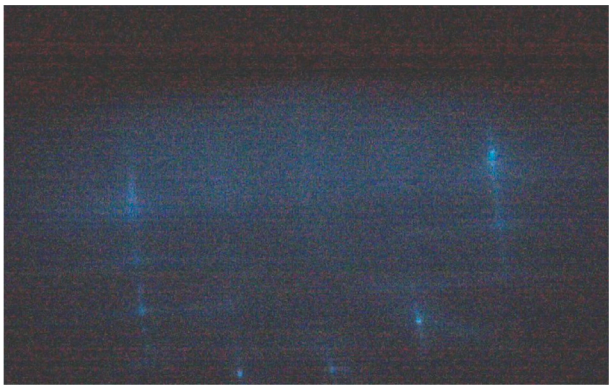

Fig. 1. Typical RHEED pattern of 4H-SiC(0001) template, showing vertical streaks from crystalline surface, horizontal Kikuchi lines from the crystal volume, and diffusive background from thin oxide layer.

After annealing, T_s was decreased (see Table 1) for (i) the GaAs heteroepitaxy (HE sample series); (ii) the deposition of Ga in the absence of As (As_4 beam equivalent pressure (BEP) measured by the ionization gauge was below 3×10^{-9} Torr) resulting in the formation of Ga droplets which then were crystallized in As atmosphere (DE sample series). We used 30 °C/min as the temperature slope rate of the thermocouple temperature, which approximately equals 21-22 °C/min for the real temperature. For HE series, after reaching the growth temperatures (580 or 300 °C), we waited 1–2 min for the temperature stabilization before opening Ga and As cells. For DE series, after reaching 400–500 °C, we waited about 30–40 min to reach above-mentioned As pressure in the chamber. After Ga deposition, we immediately decreased the temperature to 250 °C and then removed the samples from the growth chamber in the case of samples DE1-DE3, or to the As crystallization temperature, and opened As shutter and As valve immediately when the temperature reached the value.

For the sample DE10-HF, the chemical treatment in HF solution (5% vol) for 1 min before loading into the MBE chamber was performed to decrease the thickness of the oxide layer. The detailed description of the growth conditions of the samples is present in Table 1.

The sample surface morphology was analyzed *ex-situ* by atomic force microscopy (AFM) and scanning electron microscopy (SEM). AFM topography images were analyzed in tapping mode using Nanosensors SSS-NCHR sharp silicon tips capable of a lateral resolution of about 10 nm. Two SEM systems were used: JEOL JSM IT800(IS) and Raith eLINE. The accelerating voltage of JEOL SEM was set to 5 kV and 10 kV for Raith eLINE. Plane-view SEM images were acquired using the upper in-lens detector, while tilt-view (both with plane-view and cross-section stages) images were obtained with the secondary electron detector.

3. Results and discussion

3.1. RHEED of ultra-thin oxide layer on 4H-SiC(0001)

After loading the samples into the growth chamber, the surface morphology was monitored by the RHEED technique. While a bare SiC surface has different well-defined surface reconstructions [36–38], the presence of an ultra-thin oxide layer on top of the SiC in our samples confirmed by the simultaneous presence of the diffuse pattern, diffraction streaks from the SiC crystalline surface, and Kikuchi lines (see Fig. 1). The Kikuchi lines further validate an excellent crystalline quality of the SiC wafers. Importantly, such a diffraction pattern remained stable during the growth of most samples, indicating a consistent surface morphology and low density of the GaAs nanocrystals.

Moreover, for the sample DE10-HF, chemically treated in a 5% HF solution, the diffraction pattern was the same, confirming that

Table 1
Descriptions of the sample growth conditions.

Sample	T_s (°C)	Ga flux (ML/s)	As_4 BEP ($\times 10^{-6}$ Torr)	GaAs nominal thickness (nm)	Density ($\times 10^7$ cm^{-2})	% of vertically aligned NCs
HE1	580	0.23	1.2	117	3.3	0
HE2	580	0.23	2.9	117	3.4	0
HE3	580	0.23	4.8	117	1.2	0
HE4	580	0.23	11.3	117	0.7	0
HE5	300	0.2	11.3	102	–	0

Sample	T_s^{Ga} (°C)	Ga flux (ML/s)	Ga coverage (ML)	T_s^{As} (°C)	As_4 BEP ($\times 10^{-6}$ Torr)	Density ($\times 10^7$ cm^{-2})	% of vertically aligned NCs
DE1	500	0.01	2	–	–	1.2	–
DE2	450	0.01	2	–	–	6.0	–
DE3	400	0.01	2	–	–	34.1	–
DE4	450	0.01	2	450	2.9 (1 h)	7.8	7.4
DE5	450	0.01	2	450	11.3 (10 min)	9.3	9.1
DE6	450	0.01	2	300	2.9 (10 min)	6.5	8.7
DE7	450	0.01	2	300	11.3 (10 min)	9.3	8.8
DE8	450	0.01	2	300	42.0 (10 min)	8.7	11.5
DE9	450	0.01	2	150	42.0 (10 min)	7.3	0
DE10-HF	450	0.01	2	300	11.3 (10 min)	18.9	19.6
DE11	450	0.01	8	450	2.9 (1 h)	12.1	–
DE12	450	0.07	8	450	2.9 (1 h)	56.3	–

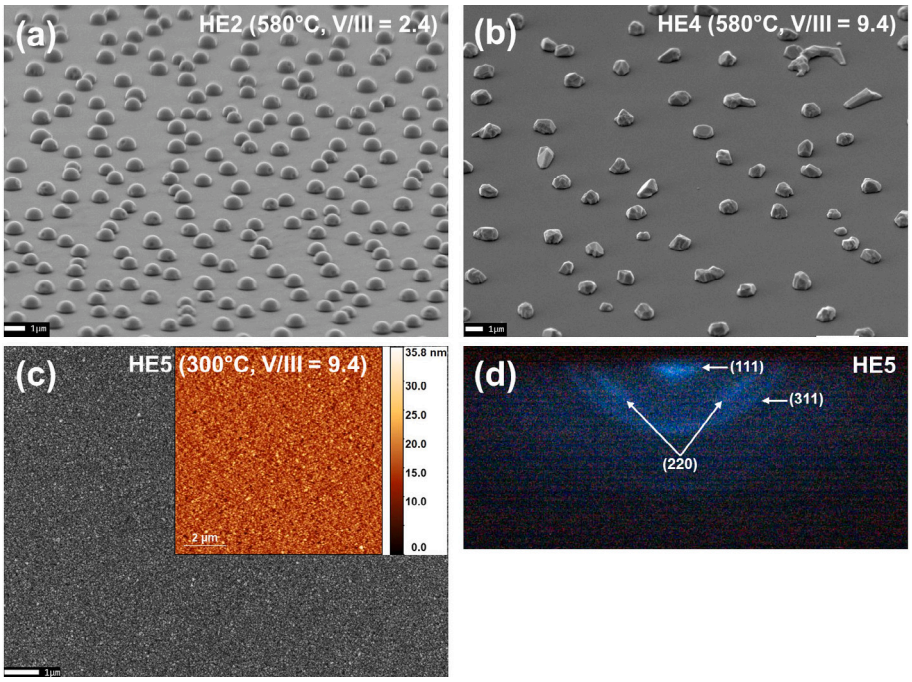

Fig. 2. Tilt-view SEM images of samples (a) HE2 (21.3 × 16 μm^2, 70° tilted angle) and (b) HE4 (25.6 × 19.2 μm^2, 60° tilted angle). (c) 12.8 × 9.6 μm^2 plane-view SEM image of sample HE5 (the inset shows 10 × 10 μm^2 AFM topography image of sample HE5), and (d) its RHEED pattern.

the oxide layer persisted after the treatment. While HF etching is a standard procedure in silicon technology for removing native oxides and achieving a hydrogen-terminated surface, it is ineffective at completely removing the last oxygen layer at the oxide/SiC interface of Si-phase 4H-SiC(0001). This results in a SiC surface with hydroxyl termination [41].

Therefore, the surface of our samples were covered with a thin oxide layer, which is essential for the fabrication of the low-density vertically-aligned III–V nanocrystals [22,23]. Due to the presence of such a RHEED pattern, the thickness of the oxide layer in both cases (with and without HF treatment) is few monolayers.

3.2. GaAs heteroepitaxy on oxide/SiC surface

In the initial series of growth experiments (HE series), GaAs was deposited at the standard growth temperature of about 580 °C typically used for the homoepitaxy on GaAs(001) or GaAs VLS growth on Si(111). The V/III ratio was varied while maintaining a constant Ga flux of approximately 0.23 ML/s (here and below 1 ML is the site-number density of the unreconstructed GaAs(001) surface, defined as 6.26× 10^{14} atoms/cm^2). The V/III ratio ranged from ≈ 1 (VLS regime) for sample HE1 to ≈ 10 (the standard value for the homoepitaxy on GaAs(001) substrates) for sample HE4. For the V/III ratio ≤ 4 (samples HE1–3), no GaAs crystal growth was observed; instead, Ga droplets with distinguished hemispherical shape formed on the surface (see Fig. 2a). Increasing the As flux promoted the formation of GaAs nanocrystals, as seen in sample HE4 by the appearance of crystalline facets (Fig. 2b). This strong dependence of GaAs crystal formation on the As flux is attributed to the lower sticking coefficient of As_4 tetramer molecules on the oxide/SiC surface compared to a bare Si surface [29]. As shown in Table 1, with an increasing V/III ratio, the density of GaAs nanocrystals slightly decreased in comparison with Ga droplets. It is expected that increasing As flux should lead to decreasing group III adatom migration length, and subsequently to increasing the

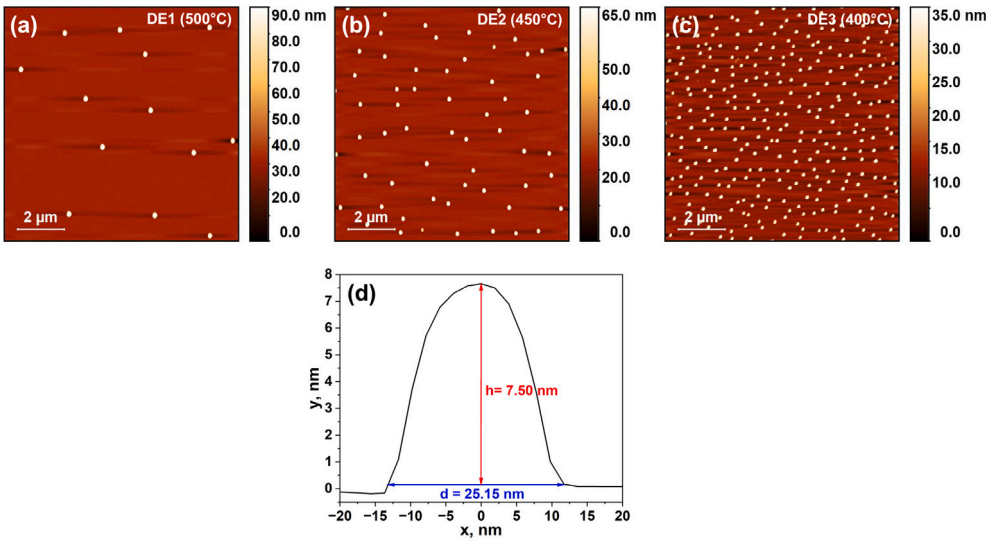

Fig. 3. 10×10 μm^2 AFM topography images of samples (a) DE1 (500 °C); (b) DE2 (450 °C); and (c) DE3 (400 °C). An elongation of droplets and black horizontal lines are AFM artefacts due to the droplet's large size and the fast scanning rate. (d) The height profile of a single droplet for sample DE1.

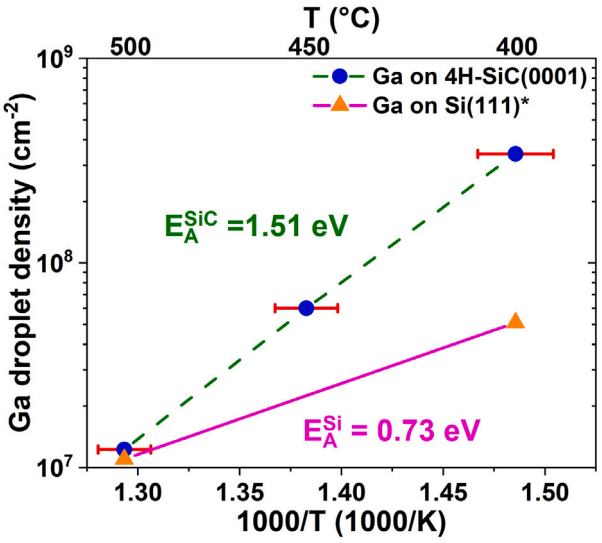

Fig. 4. Ga droplet density dependence on the substrate temperature on 4H-SiC(0001). Orange triangles are data of Ga droplets on Si(111) taken from Ref. [29].

island seed density. However, when there is no nucleation of the liquid droplets, the density of crystalline islands decreases with continuous deposition of the epitaxial material due to the ripening effects [42].

As illustrated in Fig. 2b, the GaAs nanocrystals appear poorly oriented and do not exhibit vertical alignment along the [1 1 1] direction as nanopillars typically do. However, their density is too low to allow for crystal orientation analysis using the RHEED technique, and thus, only the diffraction pattern from the oxide/SiC surface was monitored during the growth of samples HE1–4.

Our results are consistent with the previous study [19] where the direct deposition of GaAs on bare 4H-SiC at 600–650 °C leads to a formation of not-well oriented crystalline islands due to the large lattice mismatch between GaAs (a_{GaAs} = 5.65 Å) and SiC (a_{4H-SiC} = 3.07 Å) (Volmer-Weber growth mode). The difference in the morphology (mainly, the nanocrystal density) of GaAs heteroepitaxy grown at similar conditions in our work and in Ref. [19] is related to different adatom mobility on bare and oxidized SiC surface and different amounts of GaAs deposited (100 nm nominal thickness in that work and 400 nm in Ref. [19]). With continued deposition of GaAs, the nanocrystals are expected to increase in size and eventually cover the entire surface.

To study the crystallographic orientation of GaAs nanocrystals on the oxide/SiC surface, additional sample HE5 with similar Ga and As fluxes as for sample HE4 was grown at T_s of 300 °C to minimize Ga diffusion and nucleate higher density of GaAs nanocrystals. As can be seen from Fig. 2c, lower T_s leads to full covering of the SiC surface by the GaAs nanocrystals. Moreover, the RHEED pattern from a polycrystalline vertical fibre texture with the [1 1 1] axis of the sample HE5, present in Fig. 2d, confirms the preferred orientation of GaAs nanocrystals along that direction, since the diffraction pattern remains unchanged during the sample rotation [43,44]. This denotes that GaAs nanocrystals weakly interact with SiC crystal through the oxide layer, since the growth of GaAs on 4H-SiC(0001) is anticipated along the [111] direction as in the case of Si(111) surface. Nevertheless, the same crystalline state of preferred growth orientations is expected for the low-density nanocrystals obtained during GaAs heteroepitaxy in our work.

3.3. Ga droplet nucleation on oxide/SiC surface

In the second series of samples (DE series), we investigated the formation of Ga droplets on the oxide/SiC surface and their subsequent crystallization under As_4 flux. As previously noted, direct GaAs heteroepitaxy produces low-density GaAs nanocrystals with poorly controllable density and morphology, which do not meet the objectives of this study. In contrast, the DE approach enables precise control over the density and size of III–V nanostructures by nucleating group III liquid droplets in the absence of a group V atmosphere [31–33].

Firstly, we studied the temperature density dependence of Ga droplets. Fig. 3 shows AFM topography images of samples DE1, DE2, and DE3, where Ga droplets were deposited at 500, 450, and 400 °C, respectively. As previously mentioned, a higher temperature leads to a lower droplet density due to the longer migration length of Ga adatoms [29,30,32]. In Fig. 4, an Arrhenius plot of the Ga droplet density dependence reveals the Ga droplet nucleation activation energy E_a^{SiC} = 1.51 eV, consistent with a thermally activated process [45,46]. In comparison, the density dependence of Ga droplets nucleated on bare Si(111) at the same temperature range is present in Fig. 4, showing a lower value of the activation energy for Ga droplet nucleation

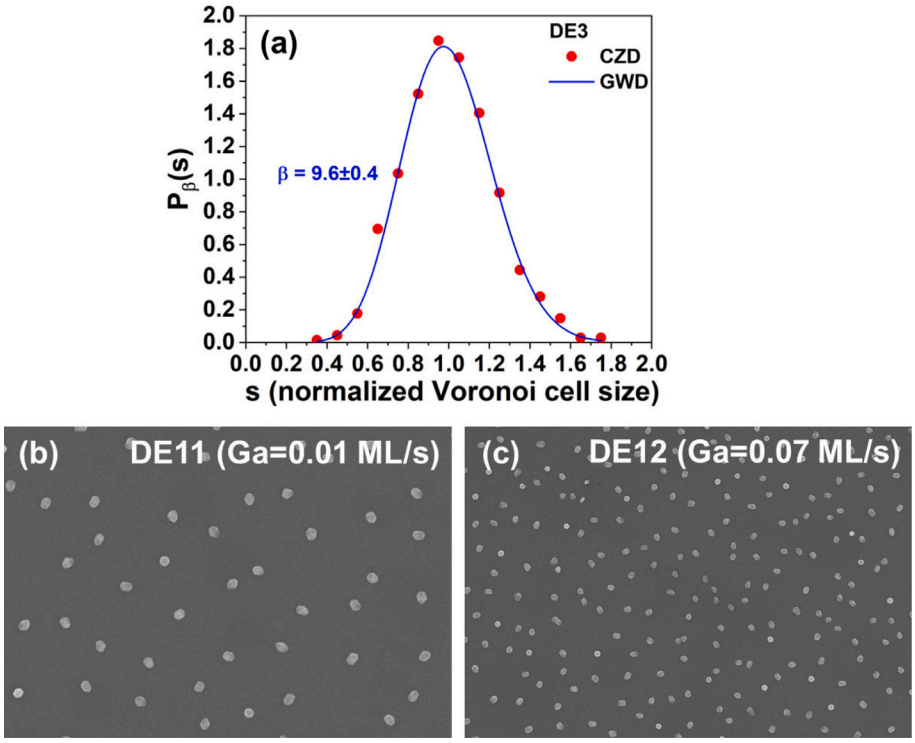

Fig. 5. (a) CZD of sample DE3 obtained from the Voronoi tessellation, fitted by GWD. (b), (c) 7.62 × 5.31 μm^2 plane-view SEM images of samples DE11–12, respectively.

(0.73 eV [29]) also in the case of Si(001) surface (0.5 eV [47]). Since it is expected that the adatom diffusion energy is smaller on the oxidized surface [48,49], the larger nucleation activation energy on oxide/SiC surface is the result of higher activation energy for the nucleation of the critical cluster and/or larger critical cluster size [45,46,50,51]. The relatively high Ga droplet nucleation energy suggests that droplet density can be effectively tuned over a broad range by adjusting the deposition temperature.

The second parameter of the nucleation process is the critical nucleus (cluster) size i - the nucleus that becomes stable (and cannot decompose into adatoms) by absorbing one additional adatom [45,46,50]. The critical size can be estimated directly from AFM images by the capture-zone distribution (CZD) approach without providing additional samples for the flux density dependence [50–53]. The capture zone (CZ) around each droplet (stable nucleus) is the area from which the adatoms are collected. CZs are determined as the cells of the Voronoi tessellation around each droplet, consisting of an area closer to that droplet than any other. The normalized CZD coincides with the generalized Wigner distribution (GWD) for the nearest-neighbor spacing distribution [50,52,53]: $P_\beta(s) = a_\beta s^\beta exp(-b_\beta s^2)$, where s is the normalized area of the CZs, a_β and b_β are the constants that guarantee normalization and unit mean conditions, respectively. The CZD approach gives access to monitor the diffusivity behavior during the nucleation process, since the fitting parameter β depends on the critical nucleus size i and the diffusion parameter γ ($\gamma = 1$ or 2 for the 2 or 1D diffusion behavior, respectively) as $\beta = \gamma i + \gamma + 1$. Fig. 5a shows experimental normalized CZD taken from the Voronoi tessellation of 15 × 15 μm^2 AFM scan for sample DE3 fitted by GWD. β equals 9.6 ± 0.4 for sample DE3, 10.1 ± 1.3 for sample DE2 (estimated from 20 × 20 μm^2 AFM scan), and 10.7 ± 2.1 for sample DE1 (estimated from 30 × 30 μm^2 AFM scan). Considering 2D adatom diffusion behavior ($\gamma = 1$) [50], the critical nucleus size equals 7–8 atoms. Such a large Ga critical nucleus size compared to 1–2 atoms on the GaAs surface [50,51,54,55] indicates weak interactions between the adatoms and the oxide/SiC surface.

As mentioned above, the critical nucleus size can be estimated from the density dependence on the flux rate [50–53]. Therefore, to evaluate critical cluster size by the second approach, two samples DE11 and DE12 were grown, where 8 ML Ga were deposited with the flux rate of 0.01 and 0.07 ML/s, respectively. For these two samples, the Ga droplets were then arsenized to crystallize them into the GaAs nanocrystals, avoiding problems related to the large droplet ripening. The morphology of samples DE11–12 are present in Fig. 5b, c. The density increased from 1.21 to 5.63 × 10^8 cm^{-2}, resulting in the exponent p of the density flux dependence ($N \propto F^p$) equals 0.79. The critical size can be estimated from the ratio: $p = \frac{i}{i+2}$ [50,52,53], leading to $i = 7.5$, coinciding with the value calculated by the CZD approach.

Another key parameter of droplets is their wetting (contact) angle, which can affect morphology, composition of nanocrystals [24,56], as well as their crystalline phase, i.e. zinc blende or wurtzite [57,58]. The contact angle is governed by interfacial surface energies and is described by the relation: $\cos\theta_c = \frac{\sigma_{SV}-\sigma_{SL}}{\sigma_{LV}}$, where θ_c is the equilibrium contact angle, σ_{SV}, σ_{SL}, and σ_{LV} are the surface tensions of the solid-vapor interface, the solid–liquid interface, and the liquid-vapor interface, respectively [59].

We estimated the wetting angle of Ga droplets by analyzing AFM images of the samples DE1–3 (see Fig. 3d). The contact angle was calculated using the spherical cap geometry model, where $\sin\theta_c = \frac{h \cdot d}{h^2 + (\frac{d}{2})^2}$. Here, h represents the droplet height, and d is the base diameter. All samples exhibited similar wetting angle with the mean values of 64.8 ± 2.2° for sample DE1, 66.6 ± 2.4° for sample DE2, and 69.5 ± 3.2° for sample DE3.

The Ga droplet wetting angle on a pure Si(111) surface is about 50° [24,60], similar to the one on GaAs(001), which does not exceed 57° [61]. By changing an oxide layer thickness on top of the Si surface, the Ga droplet wetting angle varies due to the change of the surface energy [24]. The majority of self-catalyzed GaAs NWs on Si(111) grow vertically when the thickness of the oxide layer is about 1 nm [24]. At this thickness, under given growth parameters, the oxide is sufficiently thin to prevent the formation of multiple etching sites, which would

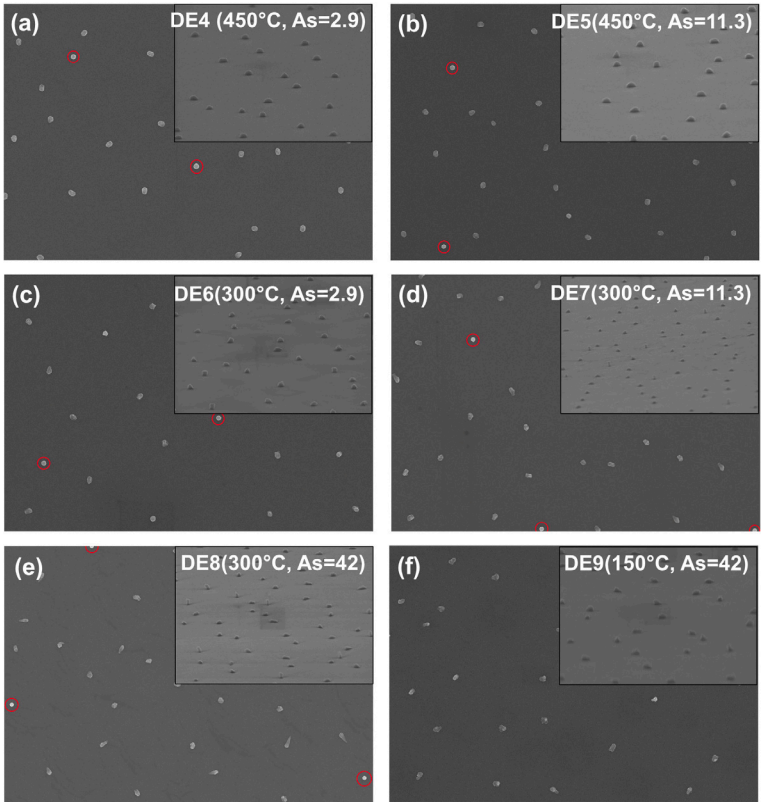

Fig. 6. 7.62 × 5.31 μm^2 plane-view and tilt-view (in the insets, 77° tilted angle) SEM images of samples with GaAs nanocrystals after the crystallization step: (a) DE4 (inset - 3.27 × 2.28 μm^2), (b) DE5 (inset - 2.61 × 1.82 μm^2), (c) DE6 (inset - 3.61 × 2.52 μm^2), (d) DE7 (inset - 5.1 × 3.59 μm^2), (e) DE8 (inset - 4.44 × 3.1 μm^2), and (f) DE9 (inset - 3.05 × 2.13 μm^2). Vertically grown GaAs nanocrystals with a hexagonal base are highlighted by the red circles on plane-view SEM images. As values in (a)–(f) are the As_4 BEP (×10^{-6} Torr).

otherwise lead to the 2D growth, but not so thick that Ga droplets are unable to effectively etch the oxide layer. If the oxide is too thick, GaAs NWs tend to crystallize in various ⟨1 1 1⟩ directions rather than growing vertically. At the optimal oxide thickness, the wetting angle of the Ga droplets is approximately 90° on oxide/Si(111), however, NWs growth remains achievable at slightly lower oxide thicknesses when the wetting angle exceeds 70–80° [24].

3.4. Arsenization of Ga droplets

The arsenization step in DE leads to crystallization of Ga liquid droplets and their transformation into the GaAs nanocrystals. Fig. 6 shows SEM images of samples DE4–9 with Ga droplets crystallized varying the temperature T_s^{As} in the range of 150–450 °C and As flux (BEP of 2.9–42.0 × 10^{-6} Torr). The GaAs nanocrystal density of samples DE4–9 is similar from sample to sample and varies in the range of 6.5–9.3 × 10^7 cm^{-2}. Nanocrystal density is mainly set during the initial Ga droplet nucleation step and it is governed by the migration length of Ga adatoms, which depends strongly on temperature (see Fig. 4). Because the droplets in samples DE4–DE9 were nucleated at the same temperature and Ga flux, the small density differences between these samples are attributed instead to variations in oxide thickness, which also influence Ga adatom diffusion.

As can be seen in in-plane SEM images of Fig. 6, DE approach in comparison with the heteroepitaxy series leads to the formation of vertically-oriented nanocrystals. Such GaAs nanocrystals have distinct hexagonal shape (highlighted by red circles) due to their well-oriented vertical facets. In tilted-view SEM images, they appear as small nanocolumns. Their typical dimensions are about 100 nm in diameter and 150—200 nm in height. These dimensions depend on the initial droplet size and on the crystallization parameters, namely temperature and As flux, since higher temperature and lower As flux tend to promote droplet diameter enlargement during the crystallization process [62]. Their amount is roughly about 10% from the total number of GaAs nanocrystals for samples DE4–DE8, and only for sample DE9 there is no formation of vertically-aligned nanocrystals for which the arsenization were carried out at low T_s^{As} of 150 °C and high As flux. It means that the etching effectively happens during the crystallization step while As is supplied, and low arsenization temperature is insufficient for Ga droplets to etch the oxide layer and reach the crystal surface of SiC to initiate the crystallization along the [111] crystallographic direction. The same happens with all the droplets crystallized not in vertical direction in samples DE4–8. The thickness of the oxide layer varies between droplets, and the experimental conditions (primarily the substrate temperature) are insufficient to effectively etch the oxide underneath the all droplet nucleation sites during the crystallization process. Only droplets that nucleate near the deepest pinholes, where the oxide layer is thinner, achieve successful oxide etching under these parameters. This selectivity explains the significant variation observed in the lateral dimensions of GaAs nanocrystals, which correlates directly with the arsenization conditions: higher temperatures and lower As fluxes enhance adatom mobility, leading to widening of the nanocrystals [14,32,63].

To validate the assumption, before loading to the MBE chamber, one sample (DE10-HF) was chemically treated in 5% HF solution to minimize the thickness of the oxide layer.

After loading the sample DE10-HF into the growth chamber, we monitored the same RHEED pattern as for the rest of the samples (see Fig. 1) suggesting the presence of the oxide layer. Ga droplet nucleation and arsenization conditions for sample DE10-HF were the same as for the sample DE7, where nanocolumn formation was observed. However, during the crystallization step of sample DE10-HF, we observed weak

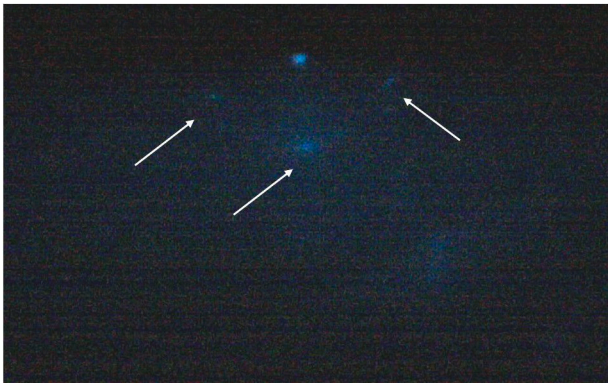

Fig. 7. The RHEED pattern during the crystallization of the sample DE10-HF. Arrows indicate short horizontal streaks originating from well-oriented vertical facets of GaAs nanocrystals.

diffraction pattern from vertically-aligned nanocrystals (see Fig. 7) meaning that their density increased, and they have the same vertical facet orientation.

Fig. 8c–h shows SEM images of the sample DE10-HF. Both, the increased total density of GaAs nanocrystals (18.9×10^7 cm^{-2}) and increased amount of vertically-aligned nanocrystals (about 20%) are related to decreased oxide layer thickness after the chemical treatment. Figs. 8e,f,g present magnified SEM images of nanocrystals with flat hexagonally shaped top surface. Their identical orientation correlates with monitored diffraction pattern and denoting that GaAs nanocrystals interact with crystalline SiC surface. A direct correlation between the preferred in-plane orientation of the hexagonal nanocrystals and the crystallographic orientation of the SiC substrate was not possible in the present study. Indeed, the RHEED patterns recorded from the vertical facets did not provide a sufficiently clear in-plane orientation fingerprint, and the SEM measurements were not referenced to the wafer primary flat. Nevertheless, the hexagonal morphology is consistent with faceting of a (111)-like zinc-blende crystal, for which the in-plane edges are expected to follow the usual $\langle 1\,\bar{1}\,0\rangle$-type and $\langle \bar{1}\,\bar{1}\,2\rangle$-type directions. The achieved density of vertically aligned GaAs nanocrystals enables further study of their integration as DNAs with 2D TMD layers and its optical properties.

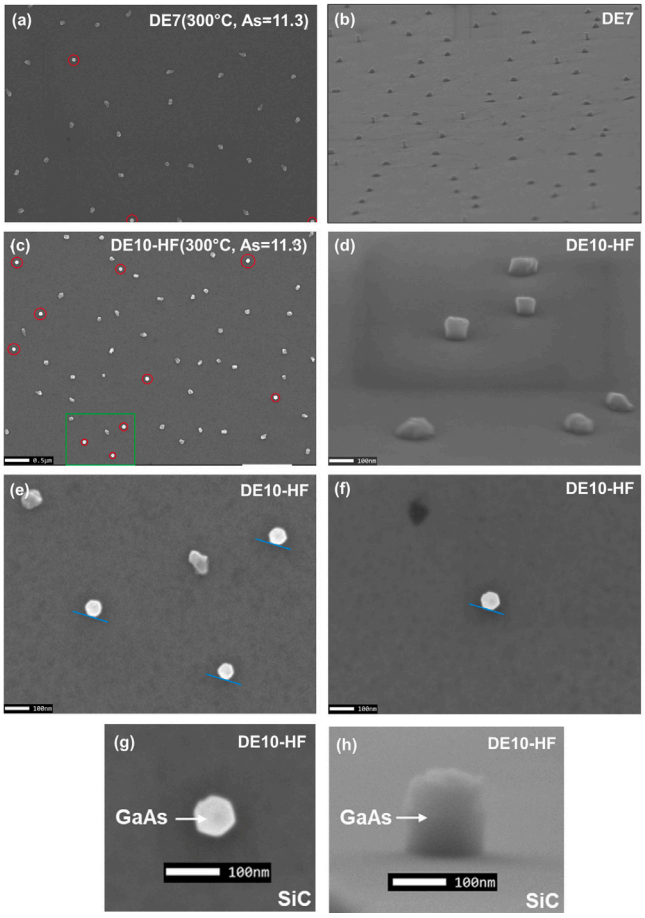

Fig. 8. (a) 7.62 × 5.31 μm² plane-view and (b) 5.1 × 3.59 μm² tilt-view (77° tilted angle) SEM images of sample DE7, same as in Fig. 6d. (c) 6.4 × 4.8 μm², (e) 1.28 × 0.96 μm², (f) 1.28 × 0.96 μm² plane-view and (d) 1.28 × 0.96 μm² tilt-view (65° tilted angle) SEM images of sample DE10-HF. Vertically grown GaAs nanocrystals with a hexagonal base are highlighted by the red circles. Image (e) is the magnified area in (c), highlighted by the green rectangle. The blue lines highlight one of the vertical facets of the GaAs nanocrystals with the hexagonal base. As values in (a) and (c) are the As_4 BEP ($\times 10^{-6}$ Torr). (g) and (h) are magnified plan-view and tilt-view SEM images of individual GaAs vertical nanoisland.

4. Conclusions

In this work, we investigated the epitaxial growth of GaAs nanocrystals on oxide-covered 4H-SiC surfaces using two distinct approaches: direct heteroepitaxy and droplet epitaxy. Our results show that conventional heteroepitaxy on oxide/SiC under typical GaAs MBE conditions produces low-density, poorly oriented nanocrystals due to limited interaction between GaAs and the underlying crystalline SiC. This led to weakly defined growth orientation and morphologies unsuitable for applications requiring vertically aligned nanostructures.

In contrast, the DE method enables precise control over nanocrystal density and vertical alignment. By optimizing arsenization conditions, we achieved self-catalyzed GaAs nanocrystals exhibiting well-defined vertical orientation. A critical parameter is the oxide layer thickness, which facilitates partial etching by Ga droplets and promotes nanowire growth along the [1 1 1] crystallographic direction.

Morphological analysis revealed a clear correlation between growth parameters, nucleation behavior, and resulting nanocrystal morphology. The large critical nucleus size for Ga droplets on oxide/SiC surfaces indicates weak substrate interaction, while wetting angle measurements suggest that the oxide thickness is close to the optimal value previously reported for the NW growth on Si(111).

CRediT authorship contribution statement

Artur Tuktamyshev: Writing – review & editing, Writing – original draft, Visualization, Validation, Project administration, Methodology, Investigation, Formal analysis, Data curation, Conceptualization. **Michele Gherardi:** Visualization, Investigation, Formal analysis, Data curation. **Luca Anzi:** Writing – review & editing, Visualization, Validation, Investigation, Data curation, Conceptualization. **Sonia Freddi:** Writing – review & editing, Visualization, Investigation, Data curation. **Matteo Canciani:** Formal analysis, Data curation. **Stefano Vichi:** Writing – review & editing, Validation, Methodology, Formal analysis. **Sergio Bietti:** Writing – review & editing, Validation. **Alexey Fedorov:** Writing – review & editing, Validation, Methodology, Formal analysis. **Monica Bollani:** Writing – review & editing, Validation, Methodology. **Roman Sordan:** Writing – review & editing, Validation, Methodology, Conceptualization. **Stefano Sanguinetti:** Writing – review & editing, Validation, Supervision, Project administration, Methodology, Conceptualization.

Funding

We acknowledge the support provided by the project funded under the National Recovery and Resilience Plan (NRRP), Mission 4 Component 2 Investment 1.3-Call for tender No. 341 of 15 March 2022 of Italian Ministry of University and Research funded by the European Union-NextGenerationEU, award number PE0000023, Concession Decree No. 1564 of 11 October 2022 adopted by the Italian Ministry of University and Research, CUP D93C22000940001, Project title 'National Quantum Science and Technology Institute' (NQSTI) and by the Horizon Europe project 2D-ADDICT (Grant ID 101223249).

Declaration of competing interest

The authors declare that they have no known competing financial interests or personal relationships that could have appeared to influence the work reported in this paper.

Data availability

Data will be made available on request.

References

[1] G. Brönstrup, N. Jahr, C. Leiterer, A. Csáki, W. Fritzsche, S. Christiansen, Optical properties of individual silicon nanowires for photonic devices, ACS Nano 4 (2010) 7113–7122, http://dx.doi.org/10.1021/nn101076t.

[2] A.I. Kuznetsov, A.E. Miroshnichenko, M.L. Brongersma, Y.S. Kivshar, B. Luk'yanchuk, Optically resonant dielectric nanostructures, Science 354 (2016) aag2472, http://dx.doi.org/10.1126/science.aag2472.

[3] C. Cruciano, D. Rocco, A. Genco, A. Tognazzi, A. Locatelli, L. Carletti, A. Fedorov, C. Trovatello, G. Di Blasio, I. Bargigia, C. Louca, P. Gubian, G. Tavani, L. Lovisolo, A. Tuktamyshev, L.C. Andreani, M. Galli, G. Cerullo, G. Leo, S. Sanguinetti, C. De Angelis, M. Bollani, Shaping the emission directivity of single quantum dots in dielectric nanodisks exploiting Mie resonances, ACS Nano 19 (2025) 3500–3509, http://dx.doi.org/10.1021/acsnano.4c13327.

[4] L. Sortino, P.G. Zotev, S. Mignuzzi, J. Cambiasso, D. Schmidt, A. Genco, M. Aßmann, M. Bayer, S.A. Maier, R. Sapienza, A.I. Tartakovskii, Enhanced light-matter interaction in an atomically thin semiconductor coupled with dielectric nano-antennas, Nat. Commun. 10 (2019) 5119, http://dx.doi.org/10.1038/s41467-019-12963-3.

[5] L. Sortino, M. Brooks, P.G. Zotev, A. Genco, J. Cambiasso, S. Mignuzzi, S.A. Maier, G. Burkard, R. Sapienza, A.I. Tartakovskii, Dielectric nanoantennas for strain engineering in atomically thin two-dimensional demiconductors, ACS Photonics 7 (2020) 2413–2422, http://dx.doi.org/10.1021/acsphotonics.0c00294.

[6] L. Chang, A. Boes, P. Pintus, J.D. Peters, M. Kennedy, W. Jin, X.-W. Guo, S.-P. Yu, S.B. Papp, J.E. Bowers, High Q resonators in the GaAs and AlGaAs on insulator platform, in: Conference on Lasers and Electro-Optics, 2019, p. SF2I.2, http://dx.doi.org/10.1364/CLEO_SI.2019.SF2I.2.

[7] W. Xie, L. Chang, H. Shu, J.C. Norman, J.D. Peters, X. Wang, J.E. Bowers, Ultrahigh-Q AlGaAs-on-insulator microresonators for integrated nonlinear photonics, Opt. Express 28 (2020) 32894–32906, http://dx.doi.org/10.1364/OE.405343.

[8] H.J. Joyce, Q.H.H. Tan, C. Jagadish, Y. Kim, J. Zou, L.M. Smith, H.E. Jackson, J.M. Yarrison-Rice, P. Parkinson, M.B. Johnston, III–V semiconductor nanowires for optoelectronic device applications, Prog. Quantum. Electron. 35 (2011) 23–75, http://dx.doi.org/10.1016/j.pquantelec.2011.03.002.

[9] A. Larrue, C. Wilhelm, G. Vest, S. Combrié, A.D. Rossi, C. Soci, Monolithic integration of III-V nanowire with photonic crystal microcavity for vertical light emission, Opt. Express 20 (2012) 7758–7770, http://dx.doi.org/10.1364/OE.20.007758.

[10] F. Glas, Critical dimensions for the plastic relaxation of strained axial heterostructures in free-standing nanowires, Phys. Rev. B 74 (2006) 121302, http://dx.doi.org/10.1103/PhysRevB.74.1213020.

[11] E. Barrigón, M. Heurlin, Z. Bi, B. Monemar, L. Samuelson, Synthesis and applications of III–V nanowires, Chem. Rev. 119 (2019) 9170–9220, http://dx.doi.org/10.1021/acs.chemrev.9b00075.

[12] G. Boras, X. Yu, H. Liu, III–V ternary nanowires on Si substrates: growth, characterization and device applications, J. Semicond. 40 (2019) 101301, http://dx.doi.org/10.1088/1674-4926/40/10/101301.

[13] V. Schmidt, J.V. Wittemann, S. Senz, U. Gösele, Silicon nanowires: a review on aspects of their growth and their electrical properties, Adv. Mater. 21 (2009) 2681–2702, http://dx.doi.org/10.1002/adma.200803754.

[14] D. Scarpellini, A. Fedorov, C. Somaschini, C. Frigeri, M. Bollani, S. Bietti, R. Nöetzel, S. Sanguinetti, Ga crystallization dynamics during annealing of self-assisted GaAs nanowires, Nanotechnology 28 (2017) 045605, http://dx.doi.org/10.1088/1361-6528/28/4/045605.

[15] T.D. Moustakas, R. Paiella, Optoelectronic device physics and technology of nitride semiconductors from the UV to the terahertz, Rep. Progr. Phys. 80 (2017) 106501, http://dx.doi.org/10.1088/1361-6633/aa7bb2.

[16] R.R. Reznik, K.P. Kotlyar, I.V. Shtrom, I.P. Soshnikov, S.A. Kukushkin, A.V. Osipov, G.E. Cirlin, MBE growth of ultrathin III–V nanowires on a highly mismatched SiC/Si(111) substrate, Semiconductors 51 (2017) 1472–1476, http://dx.doi.org/10.1134/S1063782617110252.

[17] V.O. Gridchin, R.R. Reznik, K.P. Kotlyar, A.S. Dragunova, N.V. Kryzhanovskaya, A.Y. Serov, S.A. Kukushkin, G.E. Cirlin, MBE growth of InGaN nanowires on SiC/Si(111) and Si(111) substrates: comparative analysis, Tech. Phys. Lett. 48 (2022) 24–27, http://dx.doi.org/10.21883/TPL.2022.14.52105.18894.

[18] P.A. Alekseev, M.S. Dunaevskiy, A.O. Mikhailov, S.P. Lebedev, A.A. Lebedev, I.V. Ilkiv, A.I. Khrebtov, A.D. Bouravleuv, G.E. Cirlin, Electrical properties of GaAs nanowires grown on graphene/SiC hybrid substrates, Semiconductors 52 (2018) 1611–1615, http://dx.doi.org/10.1134/S1063782618120047.

[19] S. Das, N. M. Eldose, H. Stanchu, F. Maia de Oliveira, M. Benamara, Y.I. Mazur, Z. Chen, A. Mantooth, G.J. Salamo, Epitaxial growth and characterization of GaAs (111) on 4H-SiC, J. Vac. Sci. Technol. A 42 (2024) 042702, http://dx.doi.org/10.1116/6.0003454.

[20] A. Fontcuberta i Morral, C. Colombo, G. Abstreiter, J. Arbiol, J.R. Morante, Nucleation mechanism of gallium-assisted molecular beam epitaxy growth of gallium arsenide nanowires, Appl. Phys. Lett. 92 (2008) 063112, http://dx.doi.org/10.1063/1.2837191.

[21] F. Jabeen, V. Grillo, S. Rubini, F. Martelli, Self-catalyzed growth of GaAs nanowires on cleaved Si by molecular beam epitaxy, Nanotechnology 19 (2008) 275711, http://dx.doi.org/10.1088/0957-4484/19/27/275711.

[22] F. Matteini, G. Tütüncüoglu, D. Mikulik, J. Vukajlovic-Plestina, H. Potts, J.-B. Leran, W.C. Carter, A. Fontcuberta i Morral, Impact of the Ga droplet wetting, morphology, and pinholes on the orientation of GaAs nanowires, Cryst. Growth Des. 16 (2016) 5781–5786, http://dx.doi.org/10.1021/acs.cgd.6b00858.

[23] S.M. Mostafavi Kashani, Low growth rate synthesis of GaAs nanowires with uniform size, Nano Ex. 2 (2021) 020012, http://dx.doi.org/10.1088/2632-959X/abeac8.

[24] F. Matteini, G. Tütüncüoglu, H. Potts, F. Jabeen, A. Fontcuberta i Morral, Wetting of Ga on SiO_x and its impact on GaAs nanowire growth, Cryst. Growth Des. 15 (2015) 3105–3109, http://dx.doi.org/10.1021/acs.cgd.5b00374.

[25] B. Bauer, A. Rudolph, M. Soda, A. Fontcuberta i Morral, J. Zweck, D. Schuh, E. Reiger, Position controlled self-catalyzed growth of GaAs nanowires by molecular beam epitaxy, Nanotechnology 21 (2010) 435601, http://dx.doi.org/10.1088/0957-4484/21/43/435601.

[26] A.M. Munshi, D.L. Dheeraj, V.T. Fauske, D.C. Kim, J. Huh, J.F. Reinertsen, L. Ahtapodov, K.D. Lee, B. Heidari, A.T.J. van Helvoort, B.O. Fimland, H. Weman, Position-controlled uniform GaAs nanowires on silicon using nanoimprint lithography, Nano Lett. 14 (2014) 960–966, http://dx.doi.org/10.1021/nl404376m.

[27] E.M. Sala, M. Bollani, S. Bietti, A. Fedorov, L. Esposito, S. Sanguinetti, Ordered array of Ga droplets on GaAs(001) by local anodic oxidation, J. Vac. Sci. Technol. B 32 (2014) 061206, http://dx.doi.org/10.1116/1.4901017.

[28] H. Küpers, A. Tahraoui, R.B. Lewis, S. Rauwerdink, M. Matalla, O. Krüger, F. Bastiman, H. Riechert, L. Geelhaar, Surface preparation and patterning by nano imprint lithography for the selective area growth of GaAs nanowires on Si(111), Semicond. Sci. Technol. 32 (2017) 115003, http://dx.doi.org/10.1088/1361-6641/aa8c15.

[29] C. Somaschini, S. Bietti, A. Trampert, U. Jahn, C. Hauswald, H. Riechert, S. Sanguinetti, L. Geelhaar, Control over the number density and diameter of GaAs nanowires on Si(111) mediated by droplet epitaxy, Nano Lett. 13 (2013) 3607–3613, http://dx.doi.org/10.1021/nl401404w.

[30] S. Bietti, C. Somaschini, C. Frigeri, A. Fedorov, L. Esposito, L. Geelhaar, S. Sanguinetti, Self-assisted GaAs nanowires with selectable number density on silicon without oxide layer, J. Phys. D: Appl. Phys. 47 (2014) 394002, http://dx.doi.org/10.1088/0022-3727/47/39/3940.

[31] N. Koguchi, S. Takahashi, T. Chikyow, New MBE growth method for InSb quantum well boxes, J. Cryst. Growth 111 (1991) 688–692, http://dx.doi.org/10.1016/0022-0248(91)91064-H.

[32] S. Sanguinetti, S. Bietti, N. Koguchi, Droplet epitaxy of nanostructures, in: M. Henini (Ed.), Molecular Beam Epitaxy: From Research to Mass Production, second ed., Elsevier, 2018, pp. 293–314, http://dx.doi.org/10.1016/B978-0-12-812136-8.00013-X.

[33] M. Gurioli, Z. Wang, A. Rastelli, T. Kuroda, S. Sanguinetti, Droplet epitaxy of semiconductor nanostructures for quantum photonic devices, Nat. Mater. 18 (2019) 799–810, http://dx.doi.org/10.1038/s41563-019-0355-y.

[34] J.H. Neave, B.A. Joyce, P.J. Dobson, N. Norton, Dynamics of film growth of GaAs by MBE from Rheed observations, Appl. Phys. A 31 (1983) 1–8, http://dx.doi.org/10.1007/BF00617180.

[35] J.M. Van Hove, C.S. Lent, P.R. Pukite, P.I. Cohen, Damped oscillations in reflection high energy electron diffraction during GaAs MBE, J. Vac. Sci. Technol. B 1 (1983) 741–746, http://dx.doi.org/10.1116/1.582684.

[36] X.N. Xie, K.P. Loh, Observation of a 6×6 superstructure on 6H–SiC (0001) by reflection high energy electron diffraction, Appl. Phys. Lett. 77 (2000) 3361–3363, http://dx.doi.org/10.1063/1.1328050.
[37] T. Aoyama, Y. Han, A. Ichimiya, Y. Hisada, S. Mukainakano, Structural analysis of 6H–SiC(0001) surface by RHEED rocking curves, Surf. Sci. 493 (2001) 246–252, http://dx.doi.org/10.1016/S0039-6028(01)01224-9.
[38] X. Xie, H. Wang, A. Wee, K.P. Loh, The evolution of 3×3, 6×6, $\sqrt{3} \times \sqrt{3}$R30° and $6\sqrt{3} \times 6\sqrt{3}$R30° superstructures on 6H–SiC (0001) surfaces studied by reflection high energy electron diffraction, Surf. Sci. 478 (2001) 57–71, http://dx.doi.org/10.1016/S0039-6028(00)01064-5.
[39] F.J. Ferrer, E. Moreau, D. Vignaud, D. Deresmes, S. Godey, X. Wallart, Initial stages of graphitization on SiC(000-1), as studied by phase atomic force microscopy, J. Appl. Phys. 109 (2011) 054307, http://dx.doi.org/10.1063/1.3560896.
[40] A.J. SpringThorpe, S.J. Ingrey, B. Emmerstorfer, P. Mandeville, W.T. Moore, Measurement of GaAs surface oxide desorption temperatures, Appl. Phys. Lett. 50 (1987) 77–79, http://dx.doi.org/10.1063/1.97824.
[41] S. Dhar, O. Seitz, M.D. Halls, S. Choi, Y.J. Chabal, L.C. Feldman, Chemical properties of oxidized silicon carbide surfaces upon etching in hydrofluoric acid, J. Am. Chem. Soc. 131 (2009) 16808–16813, http://dx.doi.org/10.1021/ja9053465.
[42] A. Tuktamyshev, A. Fedorov, S. Bietti, S. Tsukamoto, R. Bergamaschini, F. Montalenti, S. Sanguinetti, Reentrant behavior of the density vs. temperature of indium islands on GaAs(111)A, Nanomaterials 10 (2020) 1512, http://dx.doi.org/10.3390/nano10081512.
[43] S. Andrieu, P. Fréchard, What information can be obtained by RHEED applied on polycrystalline films? Surf. Sci. 360 (1996) 289–296, http://dx.doi.org/10.1016/0039-6028(96)00303-2.
[44] F. Tang, T. Parker, G.-C. Wang, T.-M. Lu, Surface texture evolution of polycrystalline and nanostructured films: RHEED surface pole figure analysis, J. Phys. D: Appl. Phys. 40 (2007) R427, http://dx.doi.org/10.1088/0022-3727/40/23/R01.
[45] J.A. Venables, Atomic processes in crystal growth, Surf. Sci. 299–300 (1994) 798–817, http://dx.doi.org/10.1016/0039-6028(94)90698-X.
[46] T. Michely, J. Krug, Islands, Mounds and Atoms, Springer Berlin, Heidelberg, ISBN: 978-3-540-40728-7, 2004, pp. 25–29, http://dx.doi.org/10.1007/978-3-642-18672-1.
[47] M. Bollani, S. Bietti, C. Frigeri, D. Chrastina, K. Reyes, P. Smereka, J.M. Millunchick, G.M. Vanacore, M. Burghammer, A. Tagliaferri, S. Sanguinetti, Ordered arrays of embedded Ga nanoparticles on patterned silicon substrates, Nanotechnology 25 (2014) 205301, http://dx.doi.org/10.1088/0957-4484/25/20/205301.
[48] J.E. Kruse, L. Lymperakis, S. Eftychis, A. Adikimenakis, G. Doundoulakis, K. Tsagaraki, M. Androulidaki, A. Olziersky, P. Dimitrakis, V. Ioannou-Sougleridis, P. Normand, T. Koukoula, T. Kehagias, P. Komninou, G. Konstantinidis, A. Georgakilas, Selective-area growth of GaN nanowires on SiO_2-masked Si (111) substrates by molecular beam epitaxy, J. Appl. Phys. 119 (2016) 224305, http://dx.doi.org/10.1063/1.4953594.
[49] S.C. Lee, S.R.J. Brueck, Nanoscale patterned growth assisted by surface out-diffusion of adatoms from amorphous mask films in molecular beam epitaxy, Cryst. Growth Des. 16 (2016) 3669–3676, http://dx.doi.org/10.1021/acs.cgd.6b00111.
[50] A. Tuktamyshev, A. Fedorov, S. Bietti, S. Tsukamoto, S. Sanguinetti, Temperature activated dimensionality crossover in the nucleation of quantum dots by droplet epitaxy on GaAs(111)A vicinal substrates, Sci. Rep. 9 (2019) 14760, http://dx.doi.org/10.1038/s41598-019-51161-5.
[51] A. Tuktamyshev, A. Fedorov, S. Bietti, S. Vichi, R. Tambone, S. Tsukamoto, S. Sanguinetti, Nucleation of Ga droplets self-assembly on GaAs(111)A substrates, Sci. Rep. 11 (2021) 6833, http://dx.doi.org/10.1038/s41598-021-86339-3.
[52] A. Pimpinelli, T.L. Einstein, Capture-zone scaling in island nucleation: universal fluctuation behavior, Phys. Rev. Lett. 99 (2007) 226102, http://dx.doi.org/10.1103/PhysRevLett.99.226102.
[53] A. Pimpinelli, L. Tumbek, A. Winkler, Scaling and exponent equalities in island nucleation: novel results and application to organic films, J. Phys. Chem. Lett. 5 (2014) 995–998, http://dx.doi.org/10.1021/jz500282t.
[54] C. Heyn, A. Stemmann, A. Schramm, H. Welsch, W. Hansen, Á. Nemcsics, Regimes of GaAs quantum dot self-assembly by droplet epitaxy, Phys. Rev. B 76 (2007) 075317, http://dx.doi.org/10.1103/PhysRevB.76.075317.
[55] A. Ohtake, N. Ha, T. Mano, Extremely high- and low-density of Ga droplets on GaAs{111}A,B: surface-polarity dependence, Cryst. Growth Des. 15 (2015) 485–488, http://dx.doi.org/10.1021/cg501545n.
[56] D. Ren, J. Huh, D.L. Dheeraj, H. Weman, B.-O. Fimland, Influence of pitch on the morphology and luminescence properties of self-catalyzed GaAsSb nanowire arrays, Appl. Phys. Lett. 109 (2016) 243102, http://dx.doi.org/10.1063/1.4971984.
[57] F. Panciera, Z. Baraissov, G. Patriarche, V.G. Dubrovskii, F. Glas, L. Travers, U. Mirsaidov, J.-C. Harmand, Phase selection in self-catalyzed GaAs nanowires, Nano Lett. 20 (2020) 1669–1675, http://dx.doi.org/10.1021/acs.nanolett.9b04808.
[58] T. Dursap, M. Vettori, C. Botella, P. Regreny, N. Blanchard, M. Gendry, N. Chauvin, M. Bugnet, A. Danescu, J. Penuelas, Wurtzite phase control for self-assisted GaAs nanowires grown by molecular beam epitaxy, Nanotechnology 32 (2021) 155602, http://dx.doi.org/10.1088/1361-6528/abda75.
[59] O. Carrier, D. Bonn, Contact angles and the surface free energy of solids, in: D. Brutin (Ed.), Droplet Wetting and Evaporation, Academic Press, ISBN: 978-0-12-800722-8, 2015, pp. 15–23, http://dx.doi.org/10.1016/B978-0-12-800722-8.00002-3.
[60] L. Bailly-Salins, M. Vettori, T. Dursap, P. Regreny, G. Patriarche, M. Gendry, J. Penuelas, A. Danescu, Wetting of Ga droplets in SiO_2/Si cavities: application to self-assisted GaAs nanowire growth, Cryst. Growth Des. 22 (2022) 6070–6078, http://dx.doi.org/10.1021/acs.cgd.2c00685.
[61] M. Jo, T. Mano, Y. Sakuma, K. Sakoda, Size-dependent contact angle of Ga droplets on GaAs, J. Cryst. Growth 378 (2013) 5–7, http://dx.doi.org/10.1016/j.jcrysgro.2012.12.129.
[62] S. Bietti, C. Somaschini, S. Sanguinetti, Crystallization kinetics of Ga metallic nano-droplets under As flux, Nanotechnology 24 (2013) 205603, http://dx.doi.org/10.1088/0957-4484/24/20/205603.
[63] C. Somaschini, S. Bietti, N. Koguchi, S. Sanguinetti, Fabrication of multiple concentric nanoring structures, Nano Lett. 9 (2009) 3419–3424, http://dx.doi.org/10.1021/nl901493f.